

Numerical investigation of elongated drops in a microfluidic T-junction

S. Afkhami,^{1,a)} A. M. Leshansky,^{2,b)} and Y. Renardy^{3,c)}

¹*Department of Mathematical Sciences, New Jersey Institute of Technology, Newark, New Jersey 07102, USA*

²*Department of Chemical Engineering, Technion-Israel Institute of Technology, Haifa 32000, Israel*

³*Department of Mathematics, Virginia Tech, Blacksburg, Virginia 24061, USA*

(Received 24 September 2010; accepted 10 January 2011; published online 1 February 2011)

We present a combined numerical and asymptotic approach for modeling droplets in microchannels. The magnitude of viscous forces relative to the surface tension force is characterized by a capillary number, Ca , which is assumed to be small. The numerical results successfully capture existing asymptotic solutions for the motion of drops in unconfined and confined flows; examples include the analytic Stokes flow solution for a two-dimensional inviscid bubble placed in an unbounded parabolic flow field and asymptotic formulas for slender bubbles and drops in confined flows. An extensive investigation of the accuracy of the computations is presented to probe the efficacy of the methodology and algorithms. Thereafter, numerical simulations are presented for droplet breakup in a symmetric microfluidic T-junction. The results are shown to support a proposed mechanism for breakup, driven by a pressure drop in a narrow gap between the droplet and the outer channel wall, which was formally derived in the limit $Ca^{1/5} \ll 1$ [A. M. Leshansky and L. M. Pismen, “Breakup of drops in a microfluidic T junction,” *Phys. Fluids* **21**, 023303 (2009)]. © 2011 American Institute of Physics. [doi:10.1063/1.3549266]

I. INTRODUCTION

Flows of two immiscible liquids in microchannels are often dominated by surface tension. This allows for the generation of monodisperse emulsions by moving droplets through networks of microchannels.¹ For example, droplets of controllable sizes can be produced when two immiscible fluids flow through a T-junction channel.² Despite the recent research focus on droplet-based microfluidic techniques, open questions still remain for the understanding of drop deformation and breakup in a T-junction.^{3,4} From the numerical simulation point of view, there are known subtleties with these profoundly complex phenomena. Large capillary forces combined with the effect of confinement, droplet breakup, and mechanisms that trigger the breakup are just a few of the complexities in numerical simulations. From the practical viewpoint, the question arises as to when the breakup occurs since this is a determining factor for the size distribution of daughter droplets. An important parameter is the capillary number

$$Ca = \frac{\eta_e \bar{U}}{\sigma}, \quad (1)$$

which represents the comparative effect of viscous force relative to the surface tension force, with \bar{U} being the mean velocity of the flow, σ the interfacial tension, and η_e the viscosity of the carrier liquid. Even though we address small Ca , the drop shape is far from spherical because of confinement.

We address the dynamics of the two-dimensional slender droplet in a pressure-driven flow through a microfluidic T-junction. Specifically, we model the flow regime for small $Ca < 10^{-3}$ named “shear-driven breakup.”⁵ The experiments in Ref. 5 are for two fluid pairs: (i) fluorinated oil droplets in de-ionized (DI) water with 1% w/w (weight) sodium dodecyl sulfate, interfacial tension of 15.4 mN/m, drop to matrix viscosity ratio of 1.67, range of speed of the droplet arriving at the T-junction between 5.8 and 300 $\mu\text{m/s}$, and $3 \times 10^{-4} < Ca < 1.8 \times 10^{-2}$; and (ii) DI water droplets in hexadecane with 1% w/w SPAN80 (sorbitan monooleate), interfacial tension of 5 mN/m, viscosity ratio of 0.11, range of speed from 2.4 to 165 $\mu\text{m/s}$, and $3.8 \times 10^{-3} < Ca < 0.27$. The microchannels have the cross-sectional dimensions of 80 μm high and 80 μm wide. At high confinement, the breakup for small Ca is likely caused by an increase in the upstream pressure due to lubrication flow in a thin film sandwiched between the drop and the channel wall. This breakup mechanism is flow-driven and does not rely on capillary instability proposed earlier⁶ as a potential cause of breakup. Although capillary breakup is three dimensional, the flow-driven breakup is operative in two-dimensional flow models. Another possibility is that the breakup mechanism may be similar to a central pinch-off of a drop placed in an unbounded extensional flow, albeit more complicated due to the presence of confinement. In this paper, we shall show that our direct numerical simulations of the full set of equations agree well with the two-dimensional theoretical model of Ref. 7 and the experimental data on shear-driven breakup.⁵

The mechanism of breakup in Ref. 7 concerns the two-dimensional flow where a capillary instability of a cylindrical liquid thread is not operative. The dependence of the critical droplet extension on the capillary number is therefore

^{a)}Electronic mail: shahriar@njit.edu.

^{b)}Electronic mail: lisha@technion.ac.il.

^{c)}Electronic mail: renardy@math.vt.edu.

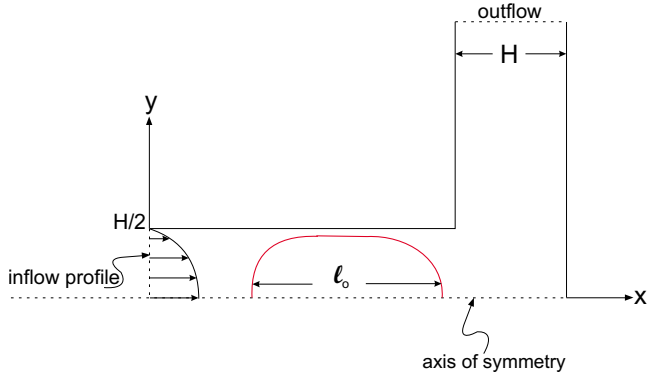


FIG. 1. (Color online) Schematic of the initial condition for numerical simulations.

based on the analysis of the lubrication flow in the narrow gap between the interface and the channel wall, where surface tension and viscous forces are assumed to be comparable. Outside this thin gap, surface tension force dominates and a simple geometric construction for the droplet shape is applied. Figure 8 of Ref. 7 is an attempt to validate the low-Ca analytical formula derived in Ref. 7 with direct numerical simulations with a volume-of-fluid (VOF) method⁸ for the maximum extension of the two-dimensional drop, ℓ , nondimensionalized by the width of the channel, w , as a function of the capillary number. The comparison is presented for an extrapolation of the theory to moderate capillary numbers because the numerical method failed at the small Ca necessary to validate the analysis,

$$\ell/w \approx 1.3 \text{ Ca}^{-0.21} \quad \text{for } \text{Ca}^{1/5} \ll 1. \quad (2)$$

Note that for $\text{Ca} < 0.02$, the theory predicts drop breakup at ℓ/w noticeably less than what is found via the numerical simulation. Thus, the physical relevance of Eq. (2) has remained open for the range of capillary numbers for which it was derived. In this paper, we shall validate this theory with direct numerical simulations in the low capillary number range. We shall begin at a slightly higher $\text{Ca} = 0.05$, where both theory and direct numerical simulations agree in Ref. 7, and decrease Ca and examine the shape from the direct numerical simulations.

II. GOVERNING EQUATIONS

We consider a drop of initial radius a and viscosity η_i in a channel of width H (see Fig. 1). The carrier liquid has a viscosity η_e and density ρ_e . The no-slip boundary condition is applied at the walls of the channel. At the inlet, a uniform normal velocity, \bar{U} , is applied with a zero gradient condition for the pressure. At the outlet, typical outflow boundary conditions, zero pressure and velocity gradient, are applied. We solve the equations of conservation of mass and momentum for two incompressible Newtonian fluids. In what follows, \mathbf{u} represents the velocity field and p the hydrodynamic pressure. We nondimensionalize the variables as follows:

$$\mathbf{x}^* = \mathbf{x}/H, \quad t^* = t\bar{U}/H, \quad \eta^* = \eta/\eta_e, \quad \rho^* = \rho/\rho_e,$$

$$\mathbf{u}^* = \mathbf{u}/\bar{U}, \quad p^* = pH/(\eta_e\bar{U}).$$

The equations of motion then become

$$\nabla^* \cdot \mathbf{u}^* = 0, \quad (3)$$

$$\begin{aligned} \text{Re} \left[\frac{\partial}{\partial t^*} (\rho^* \mathbf{u}^*) + \nabla^* \cdot (\rho^* \mathbf{u}^* \mathbf{u}^*) \right] \\ = -\nabla^* p^* + \nabla^* \cdot \boldsymbol{\tau}^* + \frac{1}{\text{Ca}} \mathbf{F}_{\text{st}}^*, \end{aligned} \quad (4)$$

where $\boldsymbol{\tau}^* = \eta^* (\nabla^* \mathbf{u}^* + \nabla^* \mathbf{u}^{*T})$ represents the dimensionless shear stress tensor, \mathbf{F}_{st}^* denotes the dimensionless body force due to surface tension, $\text{Re} = \rho_e \bar{U} H / \eta_e$ denotes the Reynolds number, and Ca is the capillary number defined by Eq. (1).

III. NUMERICAL ALGORITHM

The numerical simulation of a droplet with strong surface tension effects may be conducted with a variety of interface-tracking and interface-capturing methods.^{1,9–11} These include level set methods,¹² phase field methods,^{13,14} marker methods,¹⁵ and VOF methods,^{16–18} combined with spatial and temporal discretizations such as the boundary integral formulation,¹⁹ finite elements, and finite differences.^{20–22} A phase field method was developed in Ref. 23 and applied in Ref. 24 for a combined numerical, theoretical, and experimental study of confined droplet breakup in a T-junction with both an applied pressure gradient and a crossflow. The study includes the range of low capillary numbers that we address, but the presence of crossflow makes their analysis different from ours. Our results are obtained with an in-house code based on a VOF approach,^{18,25,26} which provides a simple way for treating topological changes of the interface. We implement the “height function” (HF) methodology, which yields a consistent representation of surface tension force. This enables an accurate computation of interface curvature, which converges with mesh refinement.^{18,27,28} Thus, the VOF-HF method is one of the recent developments that has extended the applicability of the VOF method to surface tension dominant phenomena. Below, we briefly describe the implemented VOF-HF methodology in our numerical model. For details, the reader is referred to Refs. 18, 25, 26, and 29.

In the VOF-HF methodology, the interface is locally represented as a graph in the Cartesian coordinates. The two-dimensional HF method is illustrated in Fig. 2 on a uniform mesh of size Δ . About each interface cell, in the direction most normal to the interface (estimated here by a simple finite difference evaluation of ∇f), fluid “heights” are calculated by summing volume fractions. In two dimensions, we construct either a 7×3 or a 3×7 stencil around each interface cell. For example, for the cell (i, j) illustrated in Fig. 2, $|n_y| > |n_x|$, and so the height functions are constructed by summing volume fractions vertically,

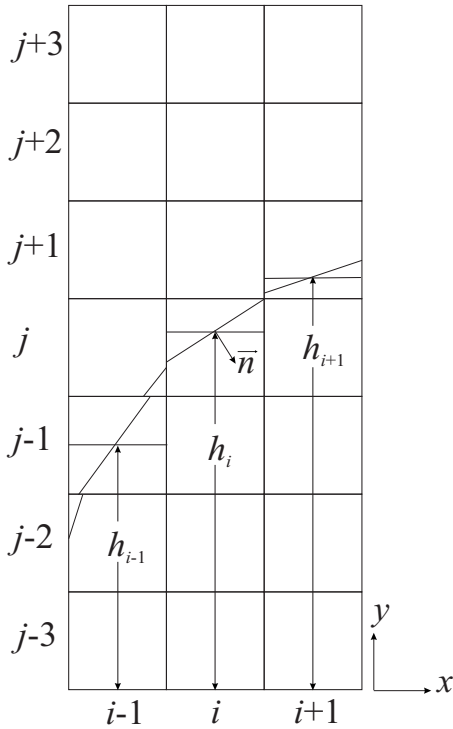


FIG. 2. The 7×3 stencil used to calculate fluid heights for the height function method.

$$h_i = \sum_{k=j-3}^{k=j+3} f_{i,k} \Delta, \quad (5)$$

with corresponding expressions for h_{i-1} and h_{i+1} . The heights h are then used to compute the interface normal \vec{n} and curvature κ at cell centers,

$$\vec{n}_{cc} = \begin{bmatrix} h_x \\ -1 \end{bmatrix}, \quad \kappa_{cc} = \frac{h_{xx}}{(1 + h_x^2)^{3/2}}, \quad (6)$$

where h_x and h_{xx} are discretized using second-order central differences. This approach yields the accuracy in curvature and surface tension force, which are essential to modeling very low capillary number flows.

The domain is discretized adaptively using the quadtree finite volumes arranged hierarchically. Primitive variables are collocated at cell centers; normal velocities are also specified at faces, as in the Marker-and-Cell (MAC) grid. The flow equations are discretized using a projection method based on a fractional-step scheme and is capable of simulating variable densities. In the fractional-step projection method, an interim velocity is computed first; this velocity field is projected onto a divergence-free velocity field, with the pressure field obtained as the solution of a Poisson equation. Advection terms are discretized using a second-order upwind scheme. As the face-centered velocities are exactly divergence-free, the volume fractions are advected using these velocities.

Next, we compare the computational results with the existing asymptotic and analytic results corresponding to the motion of deformable drops and bubbles in nonuniform unbounded and confined viscous flows. These benchmark com-

putations are an indicator of the accuracy of the implemented HF methodology in the regime of interest for the T-junction simulations that follow.

IV. BENCHMARK COMPUTATIONS

In order to validate the accuracy of our numerical model for the simulation of low capillary number flows, we have conducted the following benchmark computations. The first test is a two-dimensional inviscid bubble placed at the center of the unbounded parabolic velocity profile in Stokes flow considered by Richardson in Ref. 30. There is a one-parameter family of solutions governed by a dimensionless surface tension,

$$Z = \sigma/a^2 B \eta_e, \quad (7)$$

where $2Ba$ is the applied pressure gradient driving the flow; i.e., $B = \Delta p / (2\eta_e L)$, with a being a characteristic size of the bubble. We shall see later that Z is not simply the inverse of the capillary number, but incorporates a dimensionless measure of confinement.

The conformal mapping $z = w(\zeta)$, which maps the surface of the bubble in a complex z plane to the unit circle in the complex ζ plane, is given by Ref. 30,

$$w(\zeta) = a \left(\zeta + \frac{1}{3\zeta} + \frac{\beta}{\zeta - \alpha} \right), \quad (8)$$

where $w(\zeta)$ is analytic for $|\zeta| \geq 1$. The constants α and β are determined by numerically solving the coupled pair of equations,

$$3\beta = Z\alpha G_1(\alpha, \beta), \quad \alpha^2 - 3\beta - 1 = 2Z\alpha^2 G_2(\alpha, \beta).$$

The functions G_1 and G_2 are given by

$$G_1(\alpha, \beta) = \frac{1}{\pi} \int_0^\pi \frac{(1 - 2\alpha \cos \theta + \alpha^2)}{|P(e^{i\theta})|} d\theta,$$

$$G_2(\alpha, \beta) = \frac{1}{\pi} \int_0^\pi \frac{(\cos \theta - \alpha)}{|P(e^{i\theta})|} d\theta,$$

where $P(\zeta) = (\zeta^2 - 1/3)(\zeta - \alpha)^2 - \beta\zeta^2$. Note that for sufficiently large surface tension, the bubble has a circular cross section, so a is defined to be the radius. On the other hand, for moderate surface tension, the same value of an initial radius a in Eq. (8) would correspond to bubbles with different cross-sectional areas and a normalization would be required if bubbles of a fixed area are to be compared.

The bubble placed at the center of the parabolic flow profile is found to move faster than the undisturbed fluid velocity at the center, giving rise to a scaled bubble excess velocity,³⁰

$$\begin{aligned} \frac{U_e}{a^2 B} = & -\frac{2Z}{3\pi} \int_0^\pi \frac{(1 - 2\alpha \cos \theta + \alpha^2) \cos \theta}{|P(e^{i\theta})|} d\theta \\ & + \frac{\beta}{4\alpha^2} (1 + 3\beta) + \frac{13}{12}\beta + \frac{4}{9}. \end{aligned} \quad (9)$$

For the wall-bounded parabolic flow in a two-dimensional slit of width H , the maximum velocity of the undisturbed

parabolic flow is $U_m = H^2/8\eta_e(\Delta p/L)$. Therefore, we can write

$$Z = \frac{1}{4}(H/a)^2 Ca^{-1}, \quad (10)$$

where the capillary number, $Ca = \eta_e U_m / \sigma$, represents the comparative effect of viscous force relative to the surface tension force. The scaled bubble excess velocity can be rewritten as $U_e/(a^2 B) = \frac{1}{4}(U_e/U_m)(H/a)^2$.

The numerical simulations are carried out for a cylindrical bubble of radius a centered between parallel plates of width $H=1$ and length $L=4-8$, depending on the value of Z . The viscosity of the carrier fluid is $\eta_e=1$. The viscosity of the drop $\eta_i=0.01$ is chosen to optimize the computational cost. The densities of the two fluids are matched. The steady-state velocity is calculated from bubble displacements by averaging over the time taken by the drop to pass a distance of approximately four diameters. The mean flow velocity is $\bar{U}=1$ throughout. The Reynolds number based on the channel half width,

$$Re = \rho_e \bar{U} H / 2 \eta_e,$$

is prescribed to be 0.5 to ensure that fluid inertia is negligible for the results presented in this paper, which we have verified by repeating the simulation at $Re=0.25, 0.1$. Additionally, spatial and temporal convergence tests were conducted to ensure that the results are independent of the mesh size, time step, and the channel length.

Figures 3–5 compare the steady-state bubble shapes calculated from Eq. (8) (solid line) and the numerical simulations (dots) obtained in the finite computational domain described above. The surface tension parameter Z is varied for $a=0.075, 0.15, 0.3$. When $Z > 1$, the numerical results agree excellently with the unbounded theory for the smaller radii, $a=0.075$ and 0.15 . The comparison illustrates the manner in which confinement affects the drop shape since the computed solution is for a confined bubble, while the analytic solution is for unconfined flow. Generally, our numerical simulations show further effects of confinement where differences with the Richardson's solution arise. For smaller radii (e.g., $a=0.15$) such that the boundaries of the computational domain are sufficiently far apart, we reproduce the solution in Ref. 30; namely, at high surface tension Z , the bubble remains nearly circular as in Fig. 4(d), while at lower surface tension, the rear of the bubble fattens as in Figs. 4(a) and 4(b) toward the formation of a re-entrant cavity upon $Z \rightarrow 0$.

Figure 6 shows the dimensional velocity of the bubble as a function of surface tension for three fixed values of a . The velocity decreases as surface tension increases, as expected from the theory of Ref. 30. Another way to view the results is to recast them using Eq. (9) to compare $U_e/a^2 B$ as a function of Z . This dependence is depicted in Fig. 7. The error bars represent twice the standard deviation and indicate the uncertainty in the reported computations. Richardson's theory anticipates that for the unbounded parabolic flow the excess velocity corresponding to different a (void symbols) should collapse onto the same master curve (solid line in Fig. 7). The numerical solution shows that the bubble velocity exceeds the undisturbed maximum fluid velocity at low val-

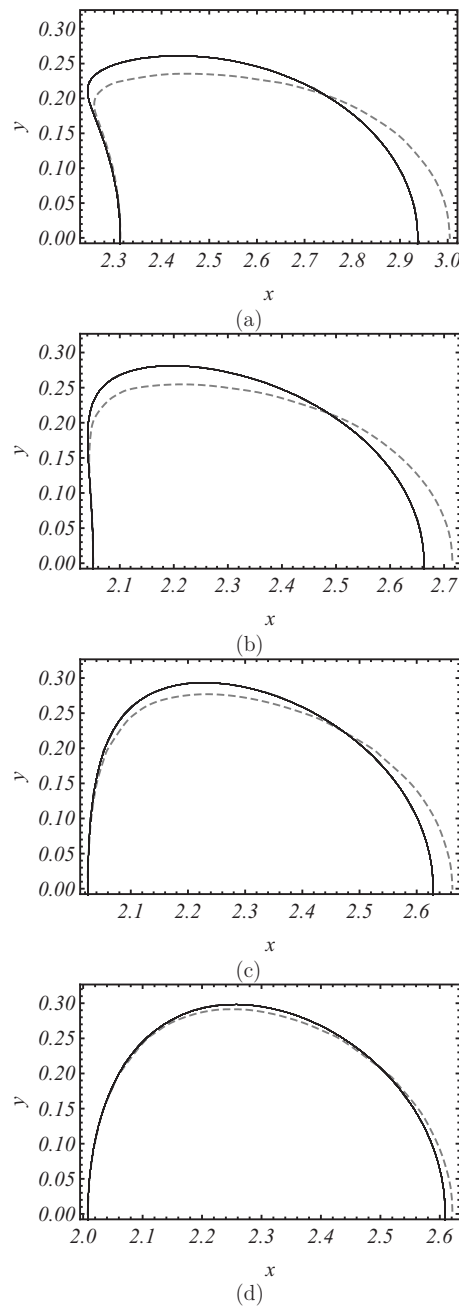


FIG. 3. Bubble shapes at the center of the parabolic velocity profile for $a=0.3$: $Z=0.93$ (a), 1.85 (b), 3.7 (c), 7.4 (d). Theoretical prediction from Eq. (8) (solid line) compared with the numerical simulations (dashed line).

ues of Z for all a , in agreement with the analytic solution (9). However, it can be readily seen in Fig. 7 that in a channel flow the excess velocity becomes negative as the surface tension Z increases. This deviation from the Richardson's theory is due to confinement and it is more pronounced for larger bubbles. Note that the retardation effect of the solid boundary on the bubble velocity at large Z is qualitatively consistent with the asymptotic solution in Ref. 31 for undeformable neutrally buoyant spherical drops, flowing axially in viscous Poiseuille flow in a cylindrical capillary: the drop was found to move slower than the maximum velocity of the undisturbed flow U_m by a factor $\sim U_m(a/R)^2$, where R is the radius of the capillary.

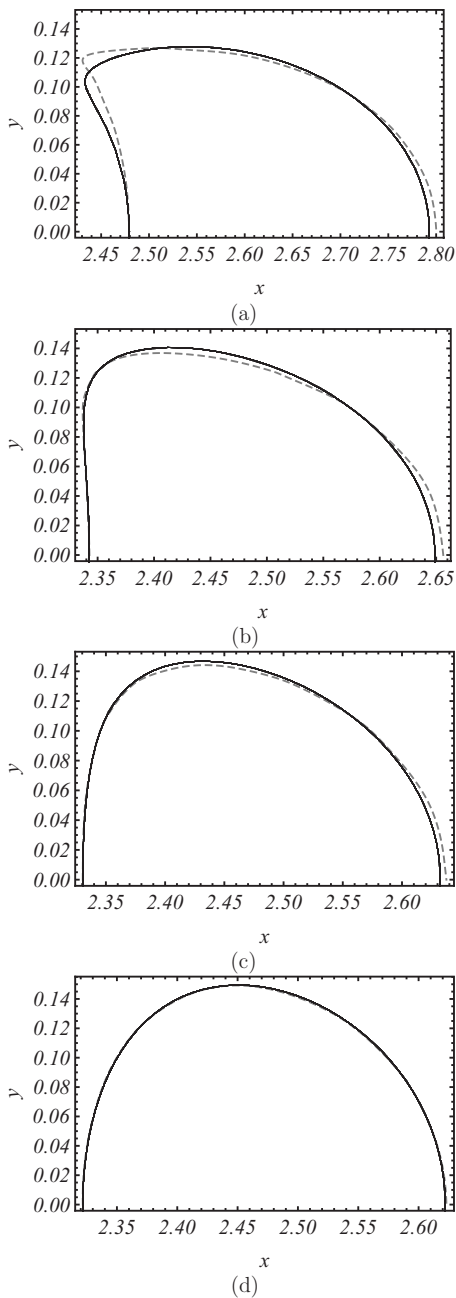


FIG. 4. Bubble shapes at the center of the parabolic velocity profile for $a=0.15$: $Z=0.74$ (a), 1.85 (b), 3.7 (c), 9.3 (d). Theoretical prediction from Eq. (8) (solid line) compared with the numerical simulations (dashed line).

We next present benchmark computations for slender bubbles and droplets in confined channels and vary the viscosity ratio and capillary number. Initially, the ratio of the drop length to the drop radius is 4, and the ratio of the droplet diameter to the channel width is 0.45. The channel width is fixed at $H=1$ and the channel length is varied from $L=5$ to 8, depending on the value of Ca . The viscosity of the carrier fluid is $\eta_e=1$, and the viscosity of the bubble is varied such that $\gamma=\eta_i/\eta_e=0.01, 0.125, 0.4, 1$. The densities of fluids are matched. Spatial and temporal convergence tests were conducted at $Re=0.1, 0.25, 0.5$ and the results were checked to be invariant with the mesh size, time step, and Reynolds numbers. In contrast to the previous benchmark computation,

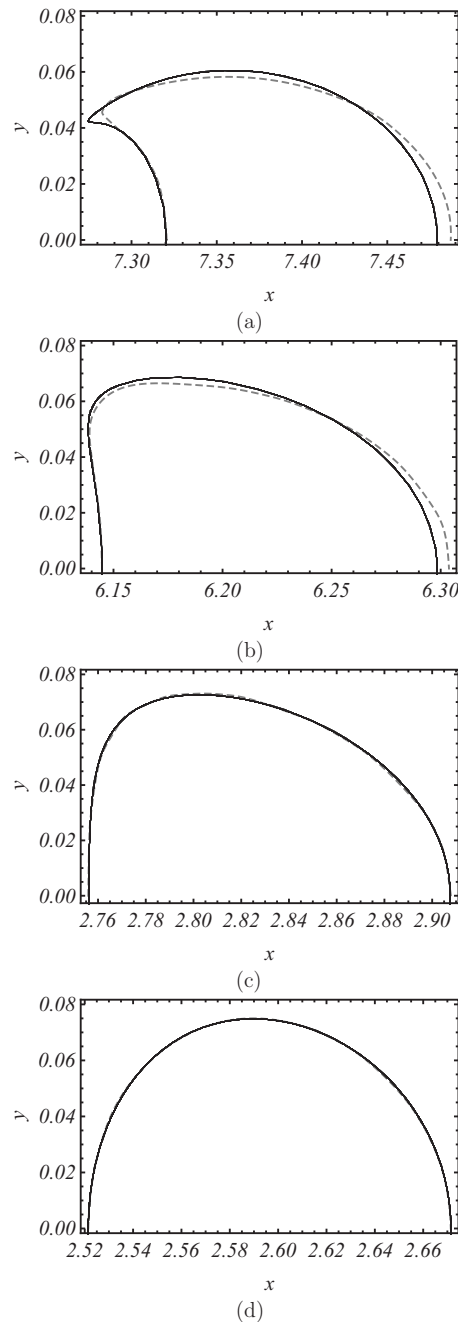


FIG. 5. Bubble shapes at the center of the parabolic velocity profile for $a=0.075$: $Z=0.3$ (a), 1.48 (b), 2.96 (c), 14.8 (d). Theoretical prediction from Eq. (8) (solid line) compared with the numerical simulations (dashed line).

grid refinement is very important to accurately capture the thin film dynamics between the drop and the wall. Specifically, the final dynamics is controlled by the flow near the wall where the circular meniscus transitions into the film. We use an adaptive mesh to focus the computations on the regions where the velocity gradient is high. The refinement between the wall and the droplet consists of at least three to four grid points vertically across that region. This is again tested for sufficiency by varying the number to five nodes. Figure 8 depicts a typical adaptive mesh utilized for the numerical simulations along with the droplet shape and the pressure distribution (color contours).

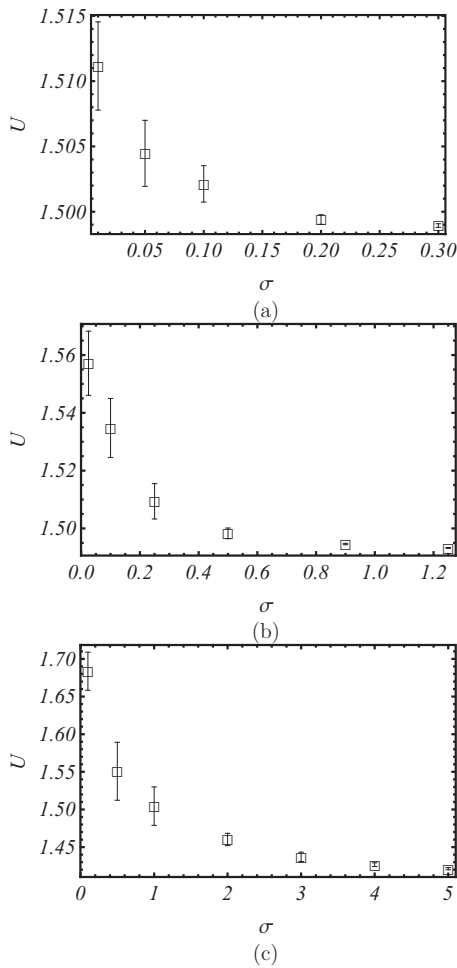


FIG. 6. Bubble dimensional velocity vs the surface tension for $\alpha=0.075$ (a), 0.15 (b), 0.3 (c).

For slow viscous flows and $Ca \ll 1$, Bretherton³² considered the method of matched asymptotic expansions for the motion of a long bubble immersed in the Poiseuille flow in a tube. He assumed a quasiunidirectional flow in the thin film sandwiched between the bubble and the tube; this lubrication approximation yielded the velocity U of the bubble immersed in the Poiseuille flow to be approximated at leading order in $Ca = \eta_e U / \sigma \ll 1$,

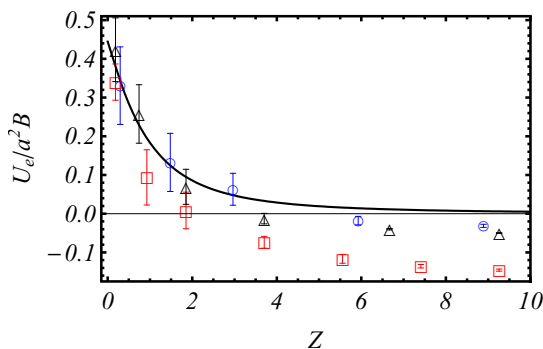


FIG. 7. (Color online) Bubble excess velocity upon varying Z , for $\alpha=0.075$ (\circ), 0.15 (\triangle), and 0.3 (\square), compared with the analytic solution in Eq. (9) (—).

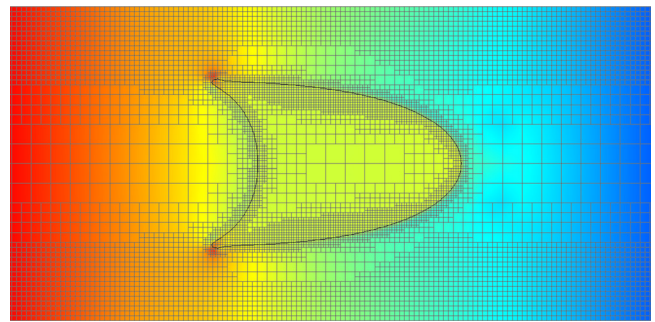


FIG. 8. (Color online) An example of the adaptive mesh utilized for the numerical simulations along with the droplet shape and the pressure distribution (color contours).

$$U/\bar{U} \approx 1 + 1.29(3\eta_e U/\sigma)^{2/3}. \tag{11}$$

This theory can be readily modified for the two-dimensional bubble placed in the Poiseuille flow between two parallel plates

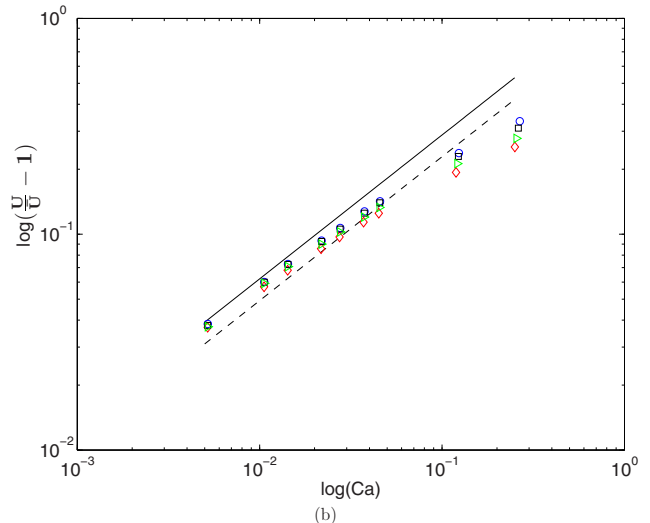
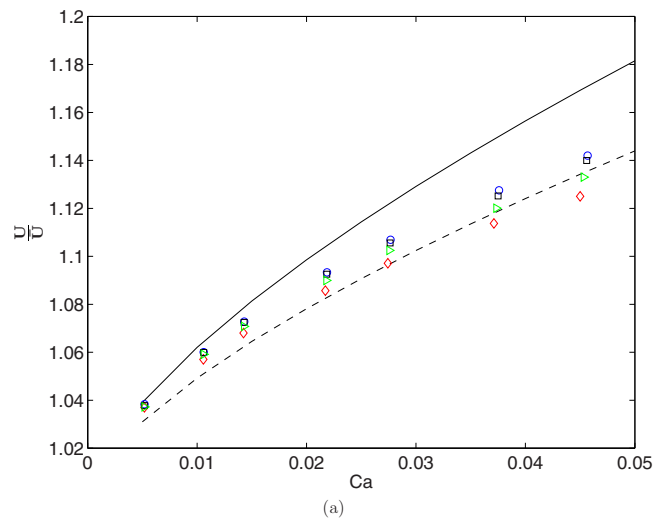


FIG. 9. (Color online) Drop velocity normalized by the mean velocity in the channel vs Ca , for $\gamma=0.01$ (\circ), 0.125 (\square), 0.4 (\triangleright), 1 (\diamond), (a) compared with asymptotic approximations given by Eq. (12) (—) and Eq. (14) (---); (b) $\log(U/\bar{U}-1)$ vs $\log Ca$.

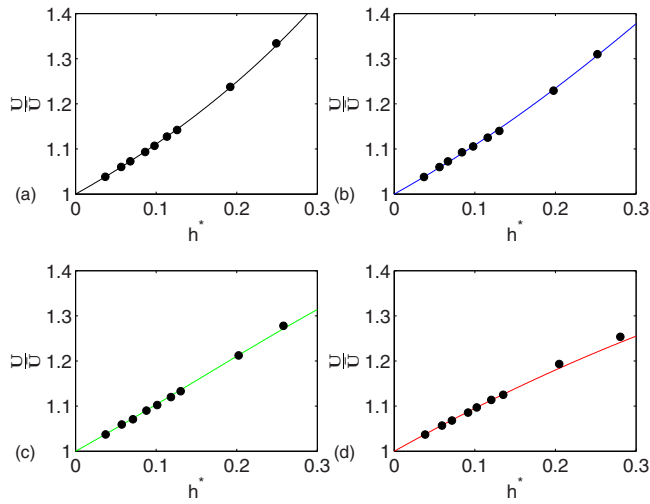


FIG. 10. (Color online) Drop velocity normalized by the mean velocity in the channel vs nondimensional film thickness h^* , for $\gamma=0.01$ (a), 0.125 (b), 0.4 (c), 1 (d); numerical results (symbols) compared with Eq. (15) (—).

$$U/\bar{U} \approx 1 + 0.643(3\eta_e U/\sigma)^{2/3}. \quad (12)$$

An extension to slender droplets with an arbitrary viscosity is given in Refs. 33 and 34, where the analytic solution for the lubrication flow in the thin film of the continuous phase is coupled to the numerical solution for the flow within the droplet. For a very viscous drop, however, the analysis of the flow in the thin film suffices and the results analogous to Eqs. (11) and (12) can readily be found as follows: the coefficients 1.29 and 0.643 in Eqs. (11) and (12), respectively, are reduced by a factor of $2^{-1/3} \approx 0.794$, yielding

$$U/\bar{U} \approx 1 + 1.02(3\eta_e U/\sigma)^{2/3} \quad (13)$$

for a bubble in a cylindrical capillary and

$$U/\bar{U} \approx 1 + 0.51(3\eta_e U/\sigma)^{2/3} \quad (14)$$

for a two-dimensional bubble in a slit channel.

Figure 9(a) shows the drop velocity normalized by the average velocity in the channel as a function of Ca at different viscosity ratios. The numerical results (symbols) agree quite well with the lubrication approximation for a bubble (—) [Eq. (12)] and a very viscous drop (---) [Eq. (14)]; the agreement is excellent for $Ca \rightarrow 0$. The predicted scaling of the $U/\bar{U} - 1$ versus Ca is demonstrated in Fig. 9(b) for varying γ .

The velocity of the slender drop can also be computed as a function of the constant film thickness h between the slender drop and the channel wall for any arbitrary viscosity. This is presented in the Appendix with an argument based on the conservation of mass. The drop velocity normalized by the mean velocity in the channel can be expressed as a function of the nondimensional film thickness $h^* = h/(H/2)$ and the viscosity ratio γ as

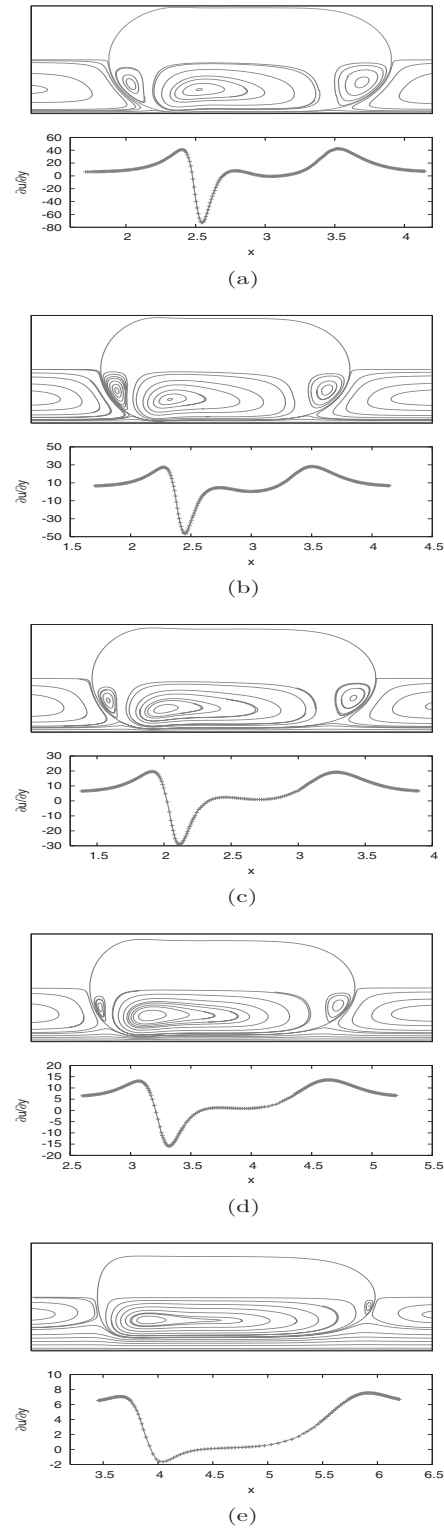


FIG. 11. Velocity streamlines in the drop in a frame of reference moving with the steady-state drop (upper plot). Shear rate $\partial u/\partial y$ along the channel wall (lower plot) for the steady states: $Ca=0.005$ (a), 0.01 (b), 0.02 (c), 0.045 (d), 0.27 (e); $\gamma=0.01$.

$$\frac{U}{\bar{U}} = \frac{1}{2} \frac{3\gamma - (3\gamma - 2)(1 - h^*)^2}{\gamma + (1 - h^*)^3 - \gamma(1 - h^*)^3}. \quad (15)$$

The film thickness and the drop velocity obtained from the numerical computations are plotted together with the predic-

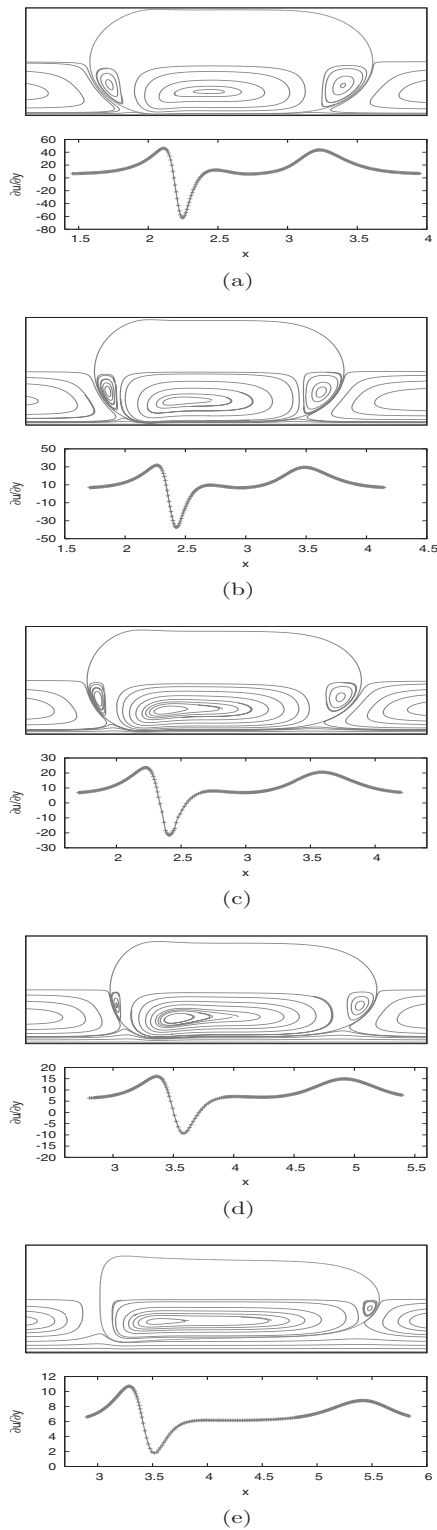


FIG. 12. Velocity streamlines in the drop in a frame of reference moving with the steady-state drop (upper plot). Shear rate $\partial u / \partial y$ along the channel wall (lower plot) for the steady states: $Ca=0.005$ (a), 0.01 (b), 0.02 (c), 0.045 (d), 0.27 (e); $\gamma=1$.

tion (15) in Fig. 10. It is evident that the comparison of numerical results with theoretical estimates is excellent, especially as $Ca \rightarrow 0$.

The upper plots in Figs. 11 and 12 show velocity streamlines in the drop frame of reference for moving interfaces

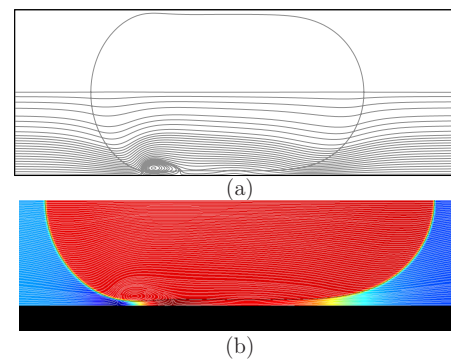


FIG. 13. (Color online) (a) Steady-state flow field in a frame of reference where the drop is moving from left to right. (b) Pressure distribution for steady states; the highest pressure gradient occurs near the stagnation point at the back of the drop: $Ca=0.01$ and $\gamma=0.01$.

which have reached steady-state shapes. An interesting observation is the mixing dynamics inside the drop in this closely fitting geometry. As shown in Fig. 9(a), the drop moves faster than the mean velocity in the channel. Therefore, there exists a region near the drop axis where the velocity is higher than the steady-state velocity of the drop, causing the formation of the vortices. The mobility of the surface of the drop gives rise to one clockwise vortex that extends to the middle of the drop accompanied by two secondary counterclockwise vortices of weaker strength, one in the front and one in the back near the stagnation points. With the increase of the capillary number, the primary vortex appears to fill the center volume of the drop, suppressing the secondary vortices. In front of the drop, a backward recirculation is formed in the channel, while at the back of the drop, the recirculating flow in the channel is forward. The flow in the thin film sandwiched between the drop and the channel wall is observed to be indeed quasiunidirectional. Two stagnation points are observed on the drop surface at the points of intersection of the backward recirculation in front of the drop and forward recirculation at the back of the drop. Figures 11 and 12 show that increasing the viscosity contrast from $\gamma=0.01$ to 1 induces a strengthening of vortices in front and at the rear of the drop, as well as the backward recirculation motion of the central vortex.

The counter-rotating primary and secondary vortices correspond to wall shear stresses with opposite signs. Figure 13(a) shows the velocity streamlines in a frame of reference where the drop is moving. Interestingly, a recirculating vortex arises due to the entrainment of the fluid as the drop moves forward. This recirculation contributes a significant effect on the distribution of the shear stress at the wall. The lower plots for each case in Figs. 11 and 12 give the wall shear rates at various capillary numbers for $\gamma=0.01, 1$. The magnitude of the maximum shear rate at the wall increases with decreasing capillary number. The corresponding increase in the shear rate is due to an increase in the pressure gradient at that point [see Fig. 13(b)]. In the entrained recirculating vortex region, the shear rate alternates the direction becoming negative, and therefore, there exists a region between the front and the rear of the drop where the shear rate

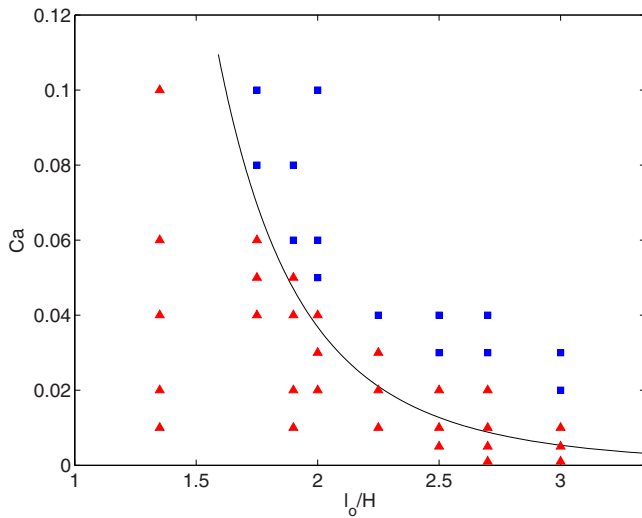


FIG. 14. (Color online) Phase diagram of numerical simulations for a drop in a symmetric T-junction. The solid line is $\ell_0/H \approx 0.98(Ca)^{-0.21}$. The symbols correspond to numerical results for nonbreaking (\triangle) and breaking (\square) drops; $\gamma=0.1$.

is zero. The shear rate away from the drop is simply that of the unperturbed Poiseuille flow.

Although the magnitude of the maximum shear rate at the wall varies significantly with the change in the capillary number, the overall behavior of the wall shear rate with respect to x is qualitatively similar at every capillary number. With increasing capillary number, the entrained recirculating vortex becomes weaker (not shown here), causing a drop in the peak of the wall shear rate, while at $Ca=0.005$, the maximum wall shear stress is almost 50 times higher than that of $Ca=0.27$.

V. DROPLET BREAKUP IN A T-JUNCTION

An open question regarding the deformation of a long drop suspended in another liquid and pushed through a T-junction is the relevance of the simplified interfacial geometry assumed by Leshansky and Pismen.⁷ The resolution of this issue requires direct numerical simulations in a difficult regime that focuses on small capillary numbers and high confinement. In this regime, the asymptotic theory in Ref. 7 has yet to be ascertained with computational results. In particular, more than one mode of drop breakup has been observed in the experimental data⁵ when a long drop goes through a T-junction.

In accordance with the experimental data in Ref. 5, the theory of Leshansky and Pismen predicts that ℓ/H scales like $Ca^{-1/5}$ and h/H scales like $Ca^{2/5}$, where ℓ is the maximum extension of the two-dimensional drop and h is the minimal film thickness between the drop and the outlet channel wall. In the limit of $Ca^{1/5} \ll 1$ and $h \ll H$, the results of their theory can be expressed as

$$\ell_0/H \approx 0.98 Ca^{-0.21}, \quad (16)$$

where ℓ_0 is the initial drop extension and

$$h/H \approx 1.08 Ca^{2/5}. \quad (17)$$

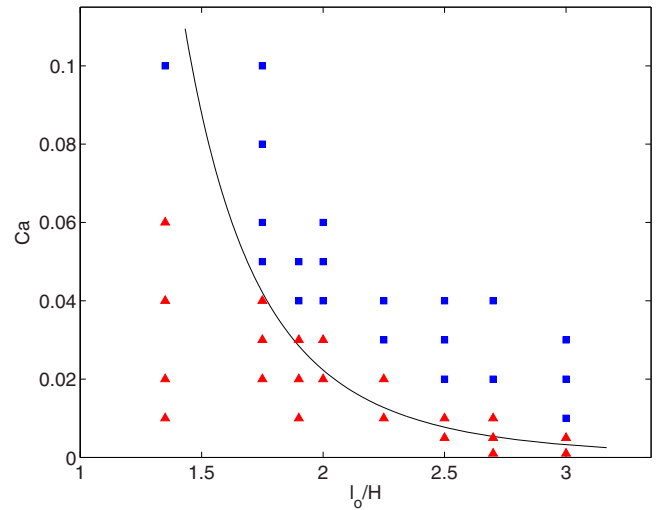


FIG. 15. (Color online) Phase diagram of numerical simulations for a drop in a symmetric T-junction. The solid line is $\ell_0/H \approx 0.9(Ca)^{-0.21}$. The symbols correspond to numerical results for nonbreaking (\triangle) and breaking (\square) drops, $\gamma=1$.

We now present the results of our computational investigation of the capillary extension and breakup of two-liquid systems in a T-junction for the initial condition sketched in Fig. 1. Our numerical experiments are compared with the theory of Ref. 7 for unprecedented low capillary numbers.

Figures 14 and 15 demonstrate the numerical calculations for viscosity ratios of $\gamma=0.1$ and $\gamma=1$ (symbols), respectively, along with Eq. (16) extrapolated to moderate values of Ca . As a whole, the numerical results agree very well with the theory for a wide range of Ca . For $\gamma=1$, we find that our numerical simulations are consistent with the predicted $(Ca)^{-0.21}$ law with a prefactor of 0.9. The experimental observations of Ref. 3 also suggest a smaller prefactor for higher viscosity drops rather than lower viscosity drops. Our simulations also reveal that drops with higher viscosity break up earlier; a possible explanation for this is the generation of higher shear stresses for drops with higher viscosities.

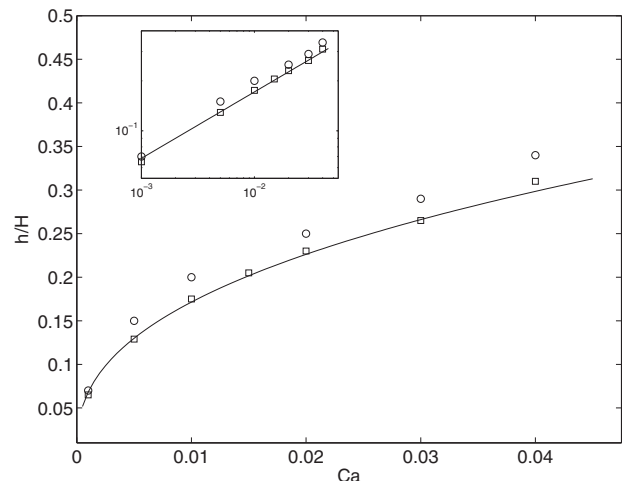


FIG. 16. Comparison of the dependence of the minimal film thickness on Ca with the thin-gap estimate of Eq. (17) (—). The symbols correspond to numerical results for $\gamma=0.1$ (\square) and $\gamma=1$ (\circ). The inset is $\log(h/H)$ vs $\log Ca$.

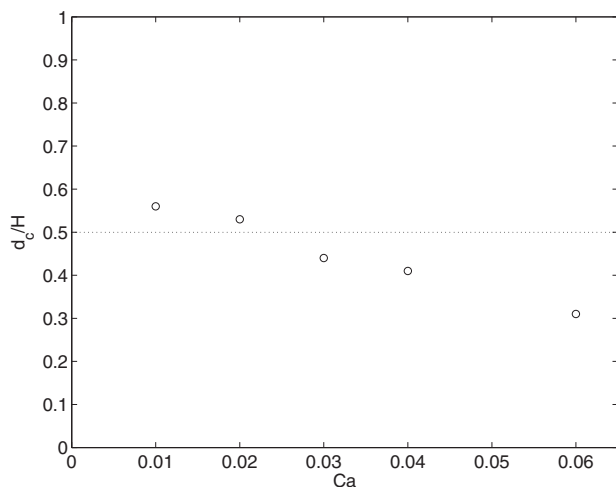


FIG. 17. The critical thickness of the neck of the drop at various capillary numbers for the nonbreaking drops closest to the breakup threshold is compared for the theoretical $d_c \approx 0.5H$ (\cdots) and full numerical simulations (\circ); $\gamma=0.1$.

We next present the dependence of the minimal film thickness h on Ca . We compare our numerical results with the theoretical prediction (17) in the limit of $h \ll H$. The scaled minimal gap thickness, h/H , as a function Ca is depicted in Fig. 16. The solid line corresponds to Eq. (17), while the inset represents the scaling of the minimal gap thickness with $(Ca)^{2/5}$ law. The agreement of the full numerical calculations with the prediction of the low- Ca theory is remarkable. It can be readily seen that for very small Ca , the numerical results coincide with the asymptotic analysis. The agreement of the theoretical law with the experimental results is already established in Ref. 5.

An additional observation proposed by the theoretical prediction in Ref. 7 is the critical width of the drop at the axis of symmetry (neck thickness) preceding breakup onset. The theory estimates the critical width d_c to be roughly $0.5H$. Figure 17 shows the computed critical thickness at various capillary numbers for the nonbreaking drops closest to the breakup threshold, and these compare well with the estimate in Ref. 7 and the experimental observations described in Ref. 5.

Figures 18(a)–18(f) illustrate the snapshots of a non-breaking drop going through a T-junction for $Ca=0.06$, $\ell_0/H=1.75$, and $\gamma=0.1$. (a) The drop is initially placed farther away from the T-junction. (b) The drop reaches the junction while slowing down. (c) The drop is pushed through the daughter channel while blocking the T-junction passage; the pressure significantly increases at the T-junction corner due to the blockage. (d) The drop is pushed further through the daughter channel due the upstream pressure; a tunnel opens up which allows the carrier liquid to flow through. (e) The drop reaches a steady state and a recirculating flow forms inside the drop. Higher velocity gradients above the drop tip and the recirculating flow inside the drop are shown in Fig. 18(f). It should be noted that due to the imposed symmetry condition, nonbreaking drops attain a steady-state configuration rather than escaping through one of the daughter channels. The case $Ca=0.06$, $\ell_0/H=1.75$, and $\gamma=0.1$ yields a

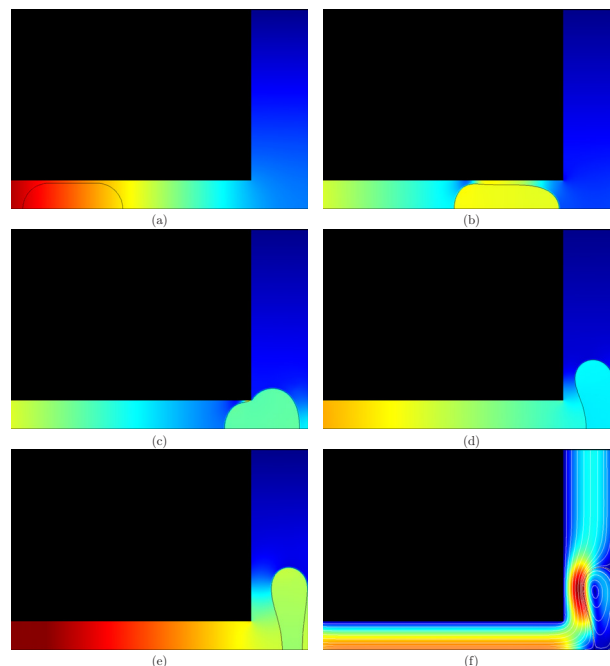


FIG. 18. (Color online) (a) Initial placement of the drop; due to symmetry, only half of the computational domain is modeled. (b) Drop arrives at the junction. (c) Drop penetrates into the T-junction, keeping the daughter channel closed. (d) Drop moves into the T-junction; a tunnel opens up. [(e) and (f)] The nonbreaking drop achieves a steady state. [(a)–(e)] The color contours illustrate the pressure distribution. (f) The steady-state velocity field and streamlines are depicted: $Ca=0.06$, $\ell_0/H=1.75$, and $\gamma=0.1$.

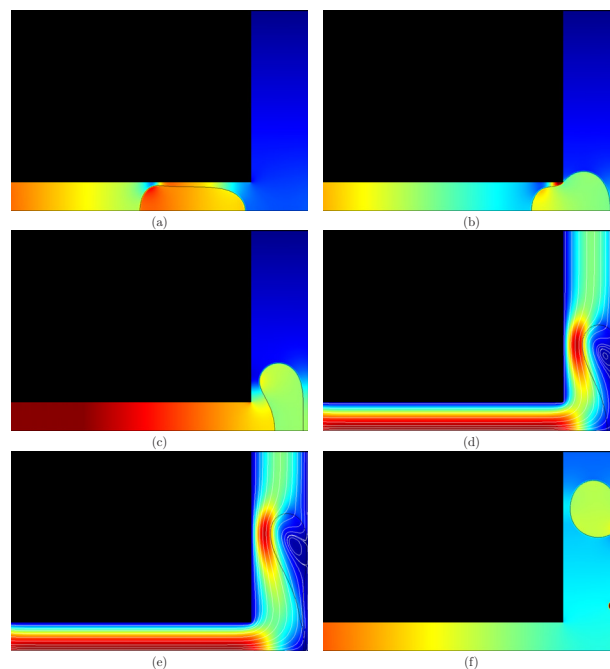


FIG. 19. (Color online) (a) Drop arrives at the junction. (b) Drop penetrates into the T-junction, keeping the daughter channel closed. (c) Drop moves into the T-junction; a tunnel opens up. (d) A neck forms while the drop is being elongated. (e) The neck thins out rapidly after its width reaches a critical thickness. (f) Drop breaks up. [(a)–(c) and (f)] The color contours illustrate the pressure distribution. [(d) and (e)] The velocity field and streamlines are depicted: $Ca=0.06$, $\ell_0/H=1.75$, and $\gamma=1$.

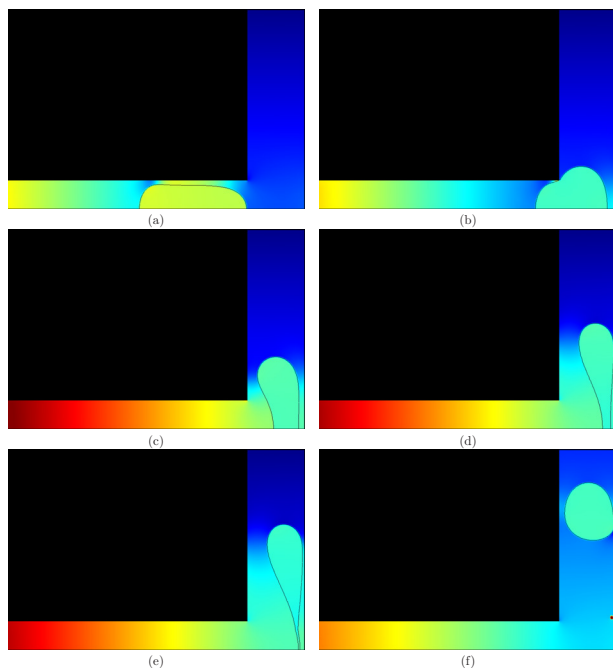


FIG. 20. (Color online) (a) The drop arrives at the junction. (b) The drop penetrates into the T-junction, keeping the daughter channel closed. (c) A tunnel opens up for the lubrication flow between the drop tip and the wall of the channel. The tunnel remains open throughout. (c) Viscous stresses build up and elongate the drop. [(d)–(f)] A neck forms and the width of the neck decreases rapidly, followed quickly by the drop breakup. The color contours illustrate the pressure distribution: $Ca=0.08$, $\ell_0/H=1.75$, and $\gamma=0.1$.

steady-state configuration, but a drop at a higher viscosity is found to break up. Figures 19(a)–19(f) illustrate the snapshots of a breaking drop for $Ca=0.06$, $\ell_0/H=1.75$, and $\gamma=1$. Higher shear stresses are shown to be responsible for elongating the higher viscosity drop more than at $\gamma=0.1$ and for the eventual breakup.

We next detail the behavior of the droplet as it goes through the T-junction preceding the breakup at $Ca=0.08$, $\ell_0/H=1.75$, and $\gamma=0.1$. A pressure-driven flow pushes the drop to penetrate into the T-junction [Fig. 20(a)]. Upon arrival at the T-junction, a tunnel of the thickness of a lubrication layer forms [Fig. 20(b)]. The tunnel remains open thereafter. An increased upstream pressure due to lubrication flow in the thin film sandwiched between the drop and the channel wall occurs next [Fig. 20(b)]. High tangential viscous stresses build up at the interface due to the lubrication flow between the droplet and the channel wall [Fig. 20(c)], resulting also in a recirculating flow inside the drop [Fig. 20(d)]. This mechanism is responsible for the elongation of the drop. A necking process kicks in after the drop is sufficiently elongated, and the drop breaks up [Fig. 20(e)]. The curvature is found to reach a constant radius at the drop tip, while the depression corresponds to a large curvature radius of the concave region. This scenario is exactly consistent with the analytical framework of Ref. 7. Figures 21–23 present the simulation results of $\ell_0/H=2$ for $Ca=0.04$ and $\gamma=0.1$, $Ca=0.04$ and $\gamma=1$, and $Ca=0.05$ and $\gamma=0.1$, respectively.

We note that Ref. 5 describes the experimental observation of a distinct regime, namely, “breakup with permanent obstruction,” in which a very long droplet obstructs the chan-

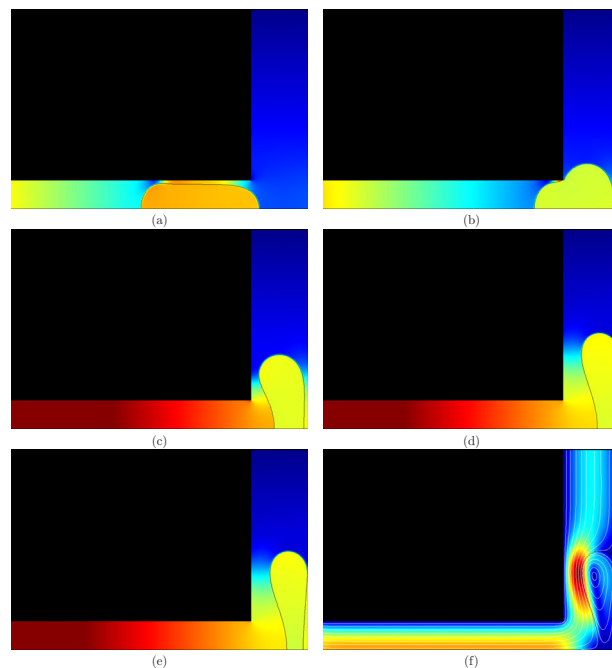


FIG. 21. (Color online) (a) The drop arrives at the junction. (b) The drop penetrates into the T-junction, keeping the daughter channel closed. (c) The drop moves into the T-junction; a tunnel opens up. [(d)–(f)] The nonbreaking drop achieves a steady state. [(a)–(e)] The color contours illustrate the pressure distribution. (f) The steady-state velocity field and streamlines are depicted: $Ca=0.04$, $\ell_0/H=2$, and $\gamma=0.1$.

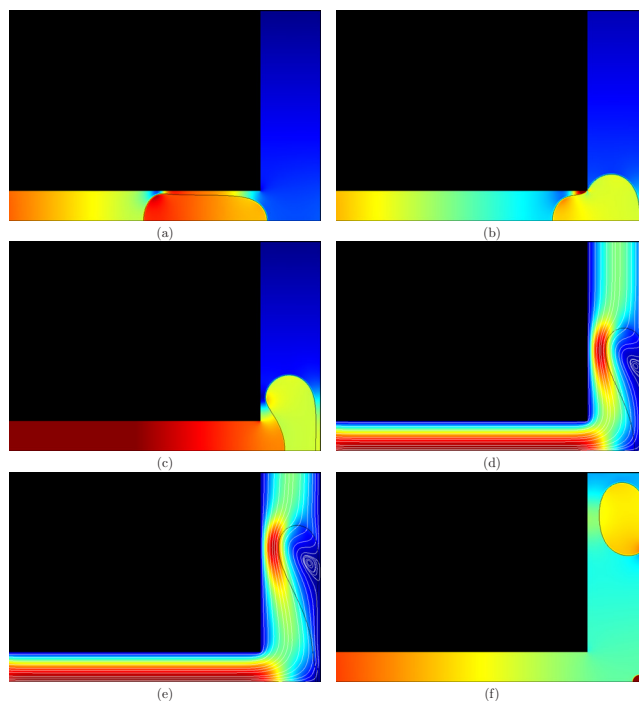


FIG. 22. (Color online) (a) The drop arrives at the junction. (b) The drop penetrates into the T-junction, keeping the daughter channel closed. (c) The drop moves into the T-junction; a tunnel opens up. (d) A neck forms while the drop is being elongated. (e) The neck thins out rapidly after its width reaches a critical thickness. (f) The drop breaks. [(a)–(c) and (f)] The color contours illustrate the pressure distribution. [(d)–(e)] The velocity field and streamlines are depicted: $Ca=0.04$, $\ell_0/H=2$, and $\gamma=1$.

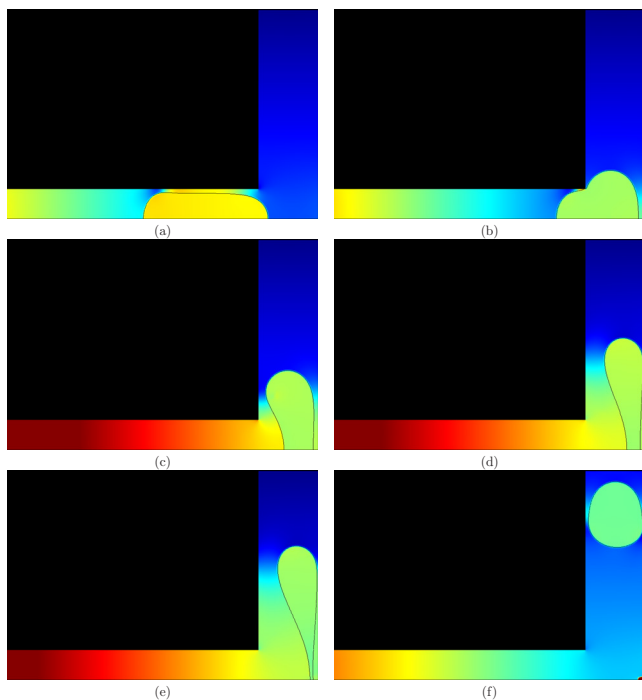


FIG. 23. (Color online) (a) The drop arrives at the junction. (b) The drop penetrates into the T-junction, keeping the daughter channel closed. (c) A tunnel opens up that allows the lubrication flow between the drop tip and the wall of the channel. The tunnel remains open throughout. (c) Viscous stresses build up elongating the drop. [(d)–(f)] A neck forms and the width of the neck decreases rapidly, followed quickly by the drop breakup. The color contours illustrate the pressure distribution: $Ca=0.05$, $\ell_0/H=2$, and $\gamma=0.1$.

nel upon entering the junction. A necking process then kicks in, followed by the drop breakup. This regime will be explored in a future investigation.

VI. CONCLUDING REMARKS

We have implemented an accurate surface tension model for the numerical simulation of drops and bubbles in microchannels. The accuracy of our numerical methodology was demonstrated by simulating benchmark problems for microflows and microdroplets with strong confinement and for various capillary numbers and viscosity ratios. Our numerical results show very good agreement with the solution of Stokes flow concerning a two-dimensional inviscid bubble placed in a parabolic flow and with asymptotic results concerning the motion and deformation of slender bubbles and drops in confined flows.

We present a combined asymptotic and numerical study of the breakup of drops through a T-junction. Minimal gap width, thickness of the neck, and breakup conditions computed numerically are consistent with the simplified model and asymptotic analysis in Ref. 7 and experimental data in Ref. 5. Our numerical simulations also agree with the estimated critical conditions for breakup. However, more than one mode of drop breakup has been observed in the experimental data of Ref. 5 when drops with very long extension go through a T-junction; this is a regime that is outside the scope of this paper.

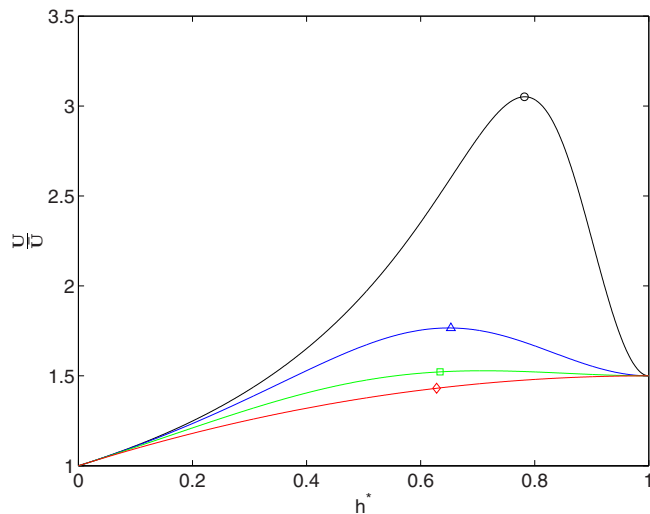


FIG. 24. (Color online) Drop velocity normalized by the mean velocity in the channel as a function of the nondimensional film thickness: $\gamma=1$ (\diamond), 0.4 (\square), 0.125 (\triangle), 0.01 (\circ).

ACKNOWLEDGMENTS

We thank Michael Renardy for insightful discussions. This research was supported in part by NSF-DMS (Grant No. 0907788), TeraGrid Large Resource Allocations (Grant Nos. TG-DMS090009 and TG-DMS090008), and the Institute for Mathematics and Its Applications at The University of Minnesota during the Fall of 2009. A.M.L. acknowledges the support of the Israel Science Foundation (ISF) via Grant No. 1319/09.

APPENDIX: 2D SLENDER DROPLET IN A CHANNEL: MASS CONSERVATION ARGUMENTS

Let the pressure gradient in a Poiseuille flow be defined as the pressure drop ΔP over length L . Let $\mathbf{v}=[u(y), 0]$ denote the pressure-driven flow between parallel plates of width W , separated by a distance H . The Navier–Stokes equations are $\eta \nabla^2 \mathbf{v} = \nabla p$, where

$$\eta u_{,yy} + \frac{\Delta P}{L} = 0. \quad (\text{A1})$$

This yields

$$u(y) = \frac{1}{2\eta} \frac{\Delta P}{L} [(H/2)^2 - y^2]. \quad (\text{A2})$$

The flow rate is

$$Q = W \int_{-H/2}^{H/2} u(y) dy = \frac{1}{12\eta} \frac{\Delta P}{L} WH^3. \quad (\text{A3})$$

The average flow rate is

$$\bar{U} = Q/HW = \frac{1}{12\eta} \frac{\Delta P}{L} H^2. \quad (\text{A4})$$

Now consider the motion of a slender drop of radius a between parallel plates of height H . The flow in the thin film

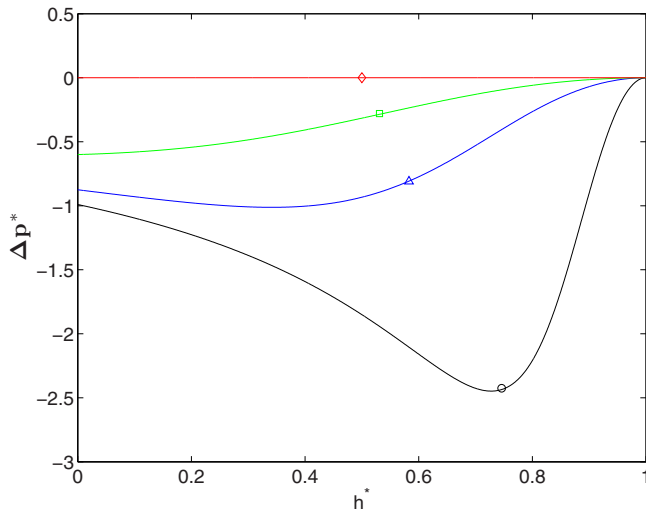


FIG. 25. (Color online) Excess pressure due to the presence of the drop, normalized by the pressure gradient in the channel in the absence of the drop, as a function of the nondimensional film thickness: $\gamma=1$ (\diamond), 0.4 (\square), 0.125 (\triangle), 0.01 (\circ).

satisfies the no-slip boundary condition at the channel wall and the continuity of velocity and shear stress at the interface; from the Poiseuille flow solution

$$u_h(y) = \frac{1}{2\eta_e} \frac{\partial p}{\partial x} [y^2 - (H/2)^2] \quad (\text{A5})$$

and

$$u_d(y) = \frac{1}{2\eta_i} \frac{\partial p}{\partial x} \left\{ y^2 - \frac{H^2}{4} [\gamma + (1-\gamma)\epsilon^2] \right\}, \quad (\text{A6})$$

where $\epsilon = a/(H/2) = 1 - h/(H/2)$, $\gamma = \eta_i/\eta_e$, and h is the film thickness between the drop and the wall. The subscripts h and d stand for the drop and the carrier liquid, respectively.

From the conservation of mass,

$$Q = Q_d + Q_h, \quad (\text{A7})$$

where

$$Q_d = 2W \int_0^a u_d(y) dy = \frac{1}{12\eta_i} \frac{\partial p}{\partial x} WH^3 \epsilon \times \left\{ \frac{1}{2} [(3\gamma - 2)\epsilon^2 - 3\gamma] \right\}, \quad (\text{A8})$$

$$Q_h = 2W \int_a^{H/2} u_h(y) dy = -\frac{1}{12\eta_i} \frac{\partial p}{\partial x} WH^3 \left[1 - \frac{3}{2}\epsilon + \frac{4}{8}\epsilon^2 \right]. \quad (\text{A9})$$

Substitution of Eqs. (A3), (A9), and (A10) into Eq. (A7) yields

$$\frac{\partial p}{\partial x} = -\frac{\Delta P}{L} \left[\frac{\gamma}{\gamma + \epsilon^3 - \gamma\epsilon^3} \right]. \quad (\text{A10})$$

The drop velocity is then

$$U_d = Q_d/(2Wa) = \bar{U} \left[\frac{1}{2} \frac{3\gamma - (3\gamma - 2)\epsilon^2}{\gamma + \epsilon^3 - \gamma\epsilon^3} \right] \quad (\text{A11})$$

using Eqs. (A4) and (A10). It is worth noting that expanding Eq. (A11) for $\epsilon \ll 1$ and using the normal stress balance at the interface also reveals that h^* scales like $Ca^{2/3}$.

Figures 24 and 25 show the drop velocity normalized by the mean velocity in the channel and the excess pressure due to the drop normalized by the pressure gradient in the channel in the absence of the drop as a function of the nondimensional film thickness $h^* = h/(H/2)$ for varying viscosity ratios.

- ¹V. Cristini and Y.-C. Tan, "Theory and numerical simulation of droplet dynamics in complex flows—A review," *Lab Chip* **4**, 257 (2004).
- ²S. L. Anna, N. Bontoux, and H. A. Stone, "Formation of dispersions using 'flow focusing' in microchannels," *Appl. Phys. Lett.* **82**, 364 (2003).
- ³P. Tabeling, "Investigating slippage, droplet breakup, and synthesizing microcapsules in microfluidic systems," *Phys. Fluids* **22**, 021302 (2010).
- ⁴V. van Steijn, C. R. Kleijn, and M. T. Kreutzer, "Flows around confined bubbles and their importance in triggering pinch-off," *Phys. Rev. Lett.* **103**, 214501 (2009).
- ⁵M.-C. Jullien, M.-J. T. M. Ching, C. Cohen, L. Menetrier, and P. Tabeling, "Droplet breakup in microfluidic T-junctions at small capillary numbers," *Phys. Fluids* **21**, 072001 (2009).
- ⁶D. R. Link, S. L. Anna, D. A. Weitz, and H. A. Stone, "Geometrically mediated breakup of drops in microfluidic devices," *Phys. Rev. Lett.* **92**, 054503 (2004).
- ⁷A. M. Leshansky and L. M. Pismen, "Breakup of drops in a microfluidic T junction," *Phys. Fluids* **21**, 023303 (2009).
- ⁸P. Urbant, "Numerical simulations of drops in microchannels," M.S. thesis, Technion, 2007.
- ⁹V. Cristini and Y. Renardy, "Scalings for droplet sizes in shear-driven breakup: Non-microfluidic ways to monodisperse emulsions," *Fluid Dyn. Mater. Process.* **2**, 77 (2006).
- ¹⁰P. Liovic, M. Francois, M. Rudman, and R. Manasseh, "Efficient simulation of surface tension-dominated flows through enhanced interface geometry interrogation," *J. Comput. Phys.* **229**, 7520 (2010).
- ¹¹M. Sussman and M. Ohta, "A stable and efficient method for treating surface tension in incompressible two-phase flow," *SIAM J. Sci. Comput. (USA)* **31**, 2447 (2009).
- ¹²X. Zheng, J. Lowengrub, A. Anderson, and V. Cristini, "Adaptive unstructured mesh. II. Application to two- and three-dimensional level-set simulations of multiphase flow," *J. Comput. Phys.* **208**, 626 (2005).
- ¹³D. M. Anderson, G. B. McFadden, and A. A. Wheeler, "Diffuse-interface methods in fluid mechanics," *Annu. Rev. Fluid Mech.* **30**, 139 (1998).
- ¹⁴P. Yue, J. J. Feng, C. Liu, and J. Shen, "A diffuse-interface method for simulating two-phase flows of complex fluids," *J. Fluid Mech.* **515**, 293 (2004).
- ¹⁵L. Duchemin, S. Popinet, and S. Zaleski, "Jet formation in bubbles bursting at a free surface," *Phys. Fluids* **14**, 3000 (2002).
- ¹⁶B. Lafaurie, C. Nardone, R. Scardovelli, S. Zaleski, and G. Zanetti, "Modelling merging and fragmentation in multiphase flows with SURFER," *J. Comput. Phys.* **113**, 134 (1994).
- ¹⁷R. Scardovelli and S. Zaleski, "Direct numerical simulation of free surface and interfacial flow," *Annu. Rev. Fluid Mech.* **31**, 567 (1999).
- ¹⁸S. Afkhami and M. Bussmann, "Height functions for applying contact angles to 2D VOF simulations," *Int. J. Numer. Methods Fluids* **57**, 453 (2008).
- ¹⁹P. J. A. Janssen and P. D. Anderson, "A boundary-integral model for drop deformation between two parallel plates with non-unit viscosity ratio drops," *J. Comput. Phys.* **227**, 8807 (2008).
- ²⁰R. Hooper, V. Cristini, S. Shakya, J. S. Lowengrub, C. W. Macosko, and J. J. Derby, "Modeling multiphase flows using a novel 3D adaptive remeshing algorithm," in *Computational Methods in Multiphase Flow*, Advances in Fluid Mechanics Vol. 29 (Wessex Institute of Technology Press, Southampton, 2001), pp. 33–42.
- ²¹P. Yue, C. Zhou, J. J. Feng, C. F. Ollivier-Gooch, and H. Hu, "Phase-field simulations of interfacial dynamics in viscoelastic fluids using finite elements with adaptive meshing," *J. Comput. Phys.* **219**, 47 (2006).
- ²²Q. Xu and O. A. Basaran, "Computational analysis of drop-on-demand

- drop formation,” *Phys. Fluids* **19**, 102111 (2007).
- ²³M. De Menech, “Modeling of droplet breakup in a microfluidic T-shaped junction,” *Phys. Rev. E* **73**, 031505 (2006).
- ²⁴M. De Menech, P. Garstecki, F. Jousse, and H. A. Stone, “Transition from squeezing to dripping in a microfluidic T-shaped junction,” *J. Fluid Mech.* **595**, 141 (2008).
- ²⁵S. Afkhami, “Applying dynamic contact angles to a three-dimensional VOF model,” Ph.D. thesis, University of Toronto, 2008.
- ²⁶S. Afkhami and M. Bussmann, “Height functions for applying contact angles to 3D VOF simulations,” *Int. J. Numer. Methods Fluids* **61**, 827 (2009).
- ²⁷S. J. Cummins, M. M. Francois, and D. B. Kothe, “Estimating curvature from volume fractions,” *Comput. Struct.* **83**, 425 (2005).
- ²⁸M. M. Francois and B. K. Swartz, “Interface curvature via volume fractions, heights and mean values on nonuniform rectangular grids,” *J. Comput. Phys.* **229**, 527 (2010).
- ²⁹S. Popinet, “Gerris: A tree-based adaptive solver for the incompressible Euler equations in complex geometries,” *J. Comput. Phys.* **190**, 572 (2003).
- ³⁰S. Richardson, “Two-dimensional bubbles in slow viscous flows. Part 2,” *J. Fluid Mech.* **58**, 115 (1973).
- ³¹G. Hetsroni, S. Haber, and E. Wacholder, “The flow fields in and around a droplet moving axially within a tube,” *J. Fluid Mech.* **41**, 689 (1970).
- ³²F. P. Bretherton, “The motion of long bubbles in tubes,” *J. Fluid Mech.* **10**, 166 (1961).
- ³³L. W. Schwartz, H. M. Princen, and A. D. Kiss, “On the motion of bubbles in capillary tubes,” *J. Fluid Mech.* **172**, 259 (1986).
- ³⁴S. R. Hodges, O. E. Jensen, and J. M. Rallison, “The motion of a viscous drop through a cylindrical tube,” *J. Fluid Mech.* **501**, 279 (2004).